Sheng-Chieh Yang, Ji-Ling Hou, Andreas Finn, Amit Kumar, Yang Ge, Wolf-Joachim Fischer

Synthesis of multifunctional plasmonic nanopillar array using soft thermal nanoimprint lithography for highly sensitive refractive index sensing

Erstveröffentlichung in / First published in:
Nanoscale. 2015, 7(13), S. 5760–5766 [Zugriff am: 04.11.2019]. Royal Society of Chemistry. ISSN 2040-3372.

DOI: https://doi.org/10.1039/c5nr00472a

Nanoscale

PAPER

View Article Online
View Journal | View Issue

Cite this: *Nanoscale*, 2015, **7**, 5760

Synthesis of multifunctional plasmonic nanopillar array using soft thermal nanoimprint lithography for highly sensitive refractive index sensing†

Sheng-Chieh Yang,*[a] Ji-Ling Hou,[b] Andreas Finn,[a] Amit Kumar,[a] Yang Ge[a] and Wolf-Joachim Fischer[a]

Received 21st January 2015,
Accepted 25th February 2015

DOI: 10.1039/c5nr00472a

www.rsc.org/nanoscale

A low-cost plasmonic nanopillar array was synthesized using soft thermal nanoimprint lithography, and its sensitivity was determined through far-field spectroscopic measurements. Its transmission spectrum was highly dependent on the refractive index of the surrounding medium, with its sensitivity being 375 nm per refractive index unit according to the spectral shift. Moreover, a simple sensor whose reflected color changed with a change in the plasma frequency on varying the surrounding medium was fabricated.

Introduction

Surface plasmon resonance (SPR)-based sensors have attracted a lot of attention over the last several decades as they allow for high-sensitivity, label-free, and high-throughput detection in real-time while consuming low sample volumes. These abilities have been exploited for different sensing applications, including for immunoassays and medical diagnostic kits, as well as the monitoring of environmental pollution.[1–4] Commercial SPR-based sensors are now available,[4] and the most common detection scheme employed in them is based on the propagation of SPR on a prism-excited Au surface owing to the phase mismatch between the incident light and the surface plasmon polaritons (SPPs) at the interface. This is known as the Kretschmann configuration,[5] in which light is focused onto the Au film and the subsequent reflection is detected. Even a slight change in the refractive index of the surface of the Au film leads to a dip shift in the angular intensity of the reflected light at the sensor surface. The resonance angle can be determined by observing the dip, which can be monitored in real-time. By monitoring the angular shift with respect to time, one can study the dynamic change in the refractive index, which is representative of the molecular binding taking place on the sensor surface. In addition to the prism coupling method, it has been reported that SPR can result from the excitation caused by a metallic grating-like nanostructure.[6] However, commercial SPR-based sensors are very expensive. Further, compared to SPR-based sensors, metallic nanostructured localized surface plasmon resonance (LSPR)-based sensors exhibit a number of advantages and are suitable alternatives to SPR-based sensors. While SPR-based sensors require a prism or a grating array to generate the SPR and must be large in area, LSPR can be generated using normal incident light, and the spot size can be reduced to the nanoscale.[7,8] Thus, LSPR-based sensors can be chip-based, low-cost, and portable point-of-care testing platforms for protein and DNA analysis.[8–10]

In recent years, research on LSPR has focused on periodic metallic subwavelength hole arrays (SWHAs). Their transmission spectra can be controlled by changing their diameter and periodicity, by rearranging the lattice, and by changing the surrounding medium.[11,12] This phenomenon is the result of the extraordinary optical transmission of the Fano resonance attributable to LSPR, which has been employed to tailor both the reflection and the transmission modes. A number of devices based on SWHAs have been reported, such as color filters and biosensors.[13–15] For thick metallic SWHA structures, previous studies have shown that transmission through the SWHAs increases with a decrease in the metal layer thickness and that saturation occurs when the thickness is down to 100 nm.[16] However, when the SWHAs have an ultrathin metal layer with a thickness comparable to the skin depth of the metal, unexpected behaviors occur. That is to say, less light penetrates through the perforated metal layer compared to that in the case of a pristine metal layer. Furthermore, strong absorption occurs in a particular range, which suppresses the

[a]*Institute of Semiconductors and Microsystems, Technische Universität Dresden, 01062 Dresden, Germany. E-mail: sheng-chieh.yang@mailbox.tu-dresden.de*
[b]*Institute of Applied Photo Physics, Technische Universität Dresden, 01069 Dresden, Germany*

†Electronic supplementary information (ESI) available: Experimental setup for measuring the transmission spectra; simulated reflectance spectrum of the metal nanodisk array; simulated reflectance spectra of PNPA structures with Ti (1 nm)/Au (23 nm) and Ti (1 nm)/Ag (20 nm)/Au (3 nm) layers: experimentally determined transmission spectra of the PNPA and the PNPA without the metal nanodisk array. See DOI: 10.1039/c5nr00472a

transmission owing to the excitation of short-range surface plasmon polaritons (SRSPPs).[17]

The fabrication of plasmonic nanostructures exhibiting controllable features, desirable dimensionalities, large-area patterns, and subwavelength spatial resolutions in a low-cost and reproducible manner is a long-term goal. Fabrication techniques such as electron-beam lithography (EBL) and the focused ion beam (FIB) method have been used to fabricate arrays of Au particles, nanoholes, and circular slits. Different shapes of various sizes can be fabricated with high precision using EBL and the FIB method.[13,14] However, it is difficult to fabricate large-area patterns using these methods, which limits their practical applicability.

Unconventional approaches such as interference lithography,[18] nanosphere lithography,[19] the template-stripping method,[20] and nanoimprint lithography (NIL)[21,22] appear to be suitable alternatives for fabricating subwavelength structures. NIL is considered an inexpensive subwavelength-region nanofabrication technique that is capable of replicating sub-10 nm features as well as complex three-dimensional (3D) structures.[22] This technique has been used widely to fabricate light-emitting diodes, thin-film transistors, and microfluidic channels.[23–25] In contrast to processes that require the use of rigid NIL molds, soft NIL using flexible molds has developed into a very promising and cost-effective method for large-scale production owing to the ease of fabrication and the reusability of the soft mold.[21]

In this study, we fabricated an enhanced-SRSPP-based plasmonic sensor by a simple and cost-effective soft thermal NIL process. We designed the plasmonic nanopillar array (PNPA) structure to allow for large-area fabrication and easy application, instead of attempting to achieve ultrahigh bulk sensitivity. When compared to conventional LSPR-based and SWHA sensors, the fabricated PNPA-based sensor exhibited comparable or even better performances. For example, the sensitivity of LSPR-based sensors is usually 120–500 nm RIU^{-1} (refractive index unit),[26–28] while that of the PNPA-based one was 375 nm RIU^{-1}. This 3D PNPA structure consisted of two types of plasmonic structures: a nanodisk array and a nanohole array (Fig. 2b). The 3D PNPA structure could couple the plasmonic modes of the nanodisk and nanohole arrays such that the sensing region, which was intrinsically highly localized and evanescent around the structures, was enlarged. As mentioned above, from the transmission spectrum, we found that the strong coupled mode resulted in an effective sensitivity of 375 nm RIU^{-1}, which is larger than that of the normal SPP mode (155.6 nm RIU^{-1}).

The reflected images were also analyzed. It has been reported that the reflectance of a plasmonic nanostructure is highly dependent on the surrounding medium and leads to color changes.[26,29] On the basis of this effect, we designed and fabricated the structures to ensure perceptible color differences in the visible range to allow for refractive index sensing. A simple refractive index sensor was fabricated, whose change in the RGB value could be observed with a change in the surrounding medium. A refractive index resolution of 4700 could be achieved.

Experimental section

A simple and low-cost soft thermal NIL process was used to fabricate the large-area nanopillar array. This array structure, which is shown in Fig. 1b, was constructed with the aim of increasing the hotspot region and thus the refractive index sensitivity. We fabricated an array of nanopillars with a diameter of 230 nm in a triangular lattice by means of soft thermal NIL. Next, we deposited a noble metal layer on the nanopillar array to act as the surface-plasmon active layer. This was done by depositing a Ti adhesion layer (1 nm), a Ag surface-plasmon active layer (20 nm), and a Au capping layer (3 nm) sequentially onto the array.

Fig. 1c–d show scanning electron microscopy (SEM) images and a digital photograph (inset) of the PNPA; the nanopillars have a periodicity of 450 nm, diameter of 230 nm, and height of 150 nm. The PNPA exhibits excellent uniformity and is fabricated over a large area. To be able to detect the change in the color of the PNPA either with a charge-coupled device (CCD) camera or through the naked eye, the thickness of the silver surface-plasmon active layer was carefully chosen on the basis of the results of a simulation described latter. This had a dramatic impact on the coupled resonant frequency, and the color reflected spontaneously. It was necessary that the reflectance cover wavelengths of 450–650 nm and have a distinct spectrum, as this would increase the perception of the color change when the spectrum red-shifted owing to an increase in the refractive index of the surrounding medium. As per our

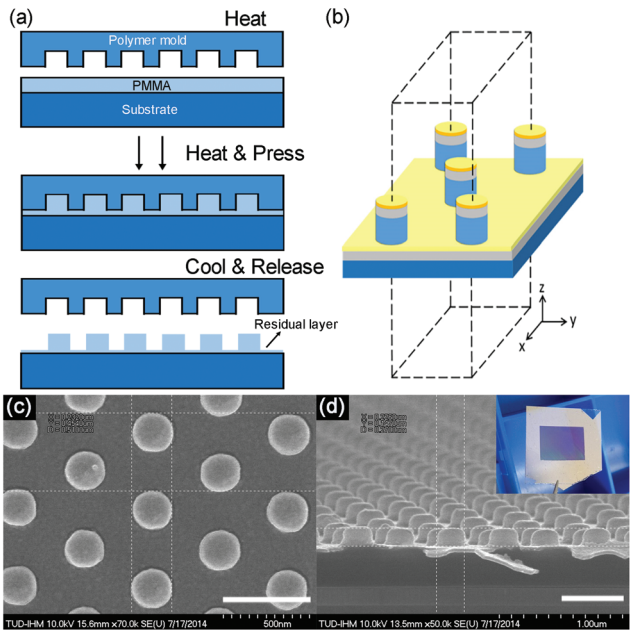

Fig. 1 (a) Schematic of the thermal NIL process. (b) Unit cell of the PNPA with a periodic boundary condition in the transverse direction. (c), (d) Top- and side-view scanning electron microscopy (SEM) images of the PNPA. The nanopillars have a diameter of 230 nm, a lattice constant of 450 nm, and a height of 150 nm. The inset shows a photograph of a typical sample (the substrate is 2 cm × 2 cm). The scale bar is 500 nm.

calculations, the thickness of the Ag surface-plasmon active layer was chosen to be 20 nm, with that of the Au capping layer being 3 nm. In this PNPA, we created two types of plasmonic nanostructures: an array of lifted metal nanodisks and an array of metal nanoholes that lay under the nanodisks. It has been reported that lifted metal disks are capable of increasing the sensitivity of refractive index sensing, as they cause a large fraction of the spatial region of the hotspot to be exposed to the environment.[30]

Results and discussion

Numerical simulation

To understand the resonant modes of the PNPA structure, we used the FDTD Solutions photonic simulation and design software (Lumerical Solutions Inc., Canada) to simulate the transmission spectra and the electric field distributions of the structure at normal incidence from the backside. Systematic simulations were performed as shown in Fig. 2. The results of the simulations were in good agreement with the experimental transmittance spectrum obtained from the corresponding peak and dip positions of the PNPA, as shown in Fig. 2b. Because the simulations were based on the ideal geometrical model, the observed deviations in the transmissions probably resulted from the differences between the model and the actual fabricated structures.

The experimental spectrum was slightly red-shifted and broader. One can attribute the red shift to the fabrication process, which inevitably would result in metal nanostructures with rounded edges, leading to a weaker resonant frequency than that in the case of perfect metal nanostructures.[31] It can be seen that there are three major peaks and dips in the simulated spectrum. In order to investigate the causes of these peaks and dips, we also performed simulations for resist nanopillar arrays with either the metal disks or the perforated metal layer, as shown in Fig. 2a, c. In all the simulated spectra, the first dip appeared at 390 nm.

Fig. 2d shows the electric field distribution at D1; we can observe clearly the diffraction pattern in the glass substrate region, meaning that the transmission dip D1 is attributable to strong reflective diffraction rather than LSPR. For dip D2, the electric field distribution (Fig. 2e) is mainly distributed in the vicinity of the perforated metal layer; this dip had a pattern similar to that of D2′ (Fig. 2g), which is from the simulation for the electric field distribution of the resist nanopillars with a perforated metal layer. Furthermore, the simulated transmission, shown in Fig. 2c, exhibits an obvious dip at the near position, indicating that D2 is caused by the perforated metal layer.

In addition, one can see that all the simulated transmission spectra exhibit a strong dip at approximately 750 nm and that the line width of D3 is broader than that of D2 (see Fig. 2b). To identify D3, the electric field distributions for all structures were simulated. It can be observed that D3″ (Fig. 2i) exhibits a strong field distribution localized around the edge, which is

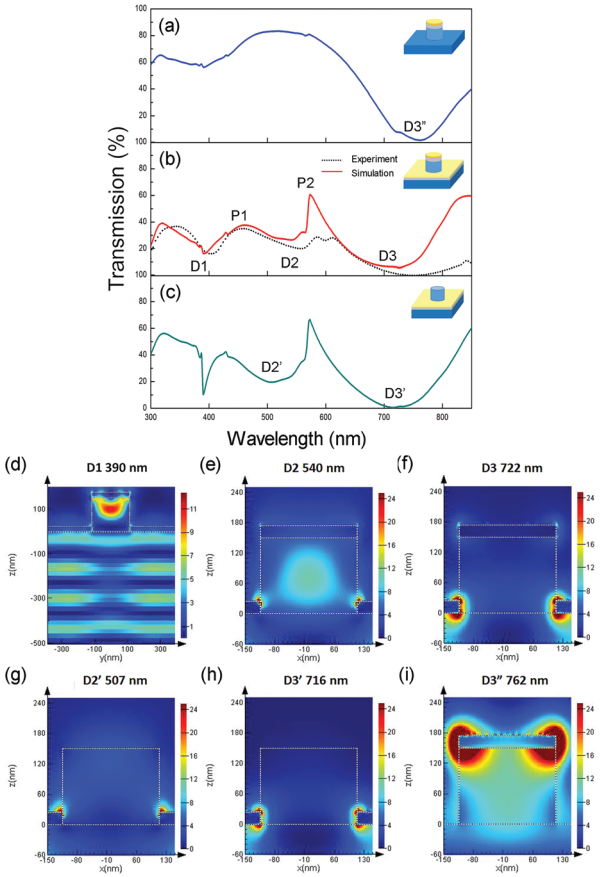

Fig. 2 (a) Simulated transmission for the structure composed of only an array of metal nanodisks without a perforated metal film. (b) Experimental (black) and simulated transmissions for the PNPA. (c) Simulated transmission for the structure composed of a resist nanopillar array and a perforated metal film. (d–i) Simulated $|E|^2$ for the peaks and dips.

believed to be caused by the strong scattering effect of the LSPR of the metal nanodisks. Meanwhile, the nanodisk array functions as a back reflector for wavelengths of 700–850 nm; this enhances the interaction between the incident light and the metal nanohole array (see ESI, Fig. S2†).

In the case of the electric field distribution of D3′ (Fig. 2h), we can see that the electric fields of both sides overlap owing to the fact that the SPPs of the two interfaces couple with each other. This phenomenon is assumed to arise from the SRSPPs when the thickness of the surface-plasmon active metal layer approaches the range of the skin depth. Certain damped SRSPPs were excited and absorbed light without re-emitting it, thus suppressing the transmission.[17] Fig. 2f shows the simulation result for D3; it can be seen that there is a localized electric field distribution around the metal disk and the hole. D3 has field features similar to those of D3′ but has a larger hotspot region; this is believed to be caused by the interference between the LSPR of the upper metal nanodisks and the SRSPPs of the bottom metal nanoholes. Compared to the hotspot regions of D1 and D2, that of D3 has a larger free-space region accessible to the sensing medium, owing to

better surface plasmon matching and enhanced SRSPP coupling; this led to higher sensitivity.

Furthermore, if one carefully considers the transmission peaks, it can be seen that the structure exhibits two primary peaks, P1 and P2, located at similar positions to those of the metal nanohole array, as shown in Fig. 2c. Both the peaks, that is, P1 and P2, can be assigned to SPP Bloch wave (SPP-BW) excitation at the interface between the metal layer and the substrate for modes (1,1) and (1,0), respectively. In the case of this PNPA structure, the optical transmission is dominated by the nanohole array.

As mentioned previously, the thickness of the Ag surface-plasmon active layer was carefully chosen to correspond to the resonant frequency, so that the differences in the color of the sensor were readily perceptible, allowing for sensing through color change. The reflectance of the PNPA with the Ag(20 nm)/Au(3 nm) layers exhibited stronger intensity and distinct features, in contrast to that of the PNPA with the Au film (23 nm) alone (see ESI, Fig. S3†). Thus, we can expect that a decrease in the intensity of red with an increase in the refractive index of the surrounding medium. The experimental results for the bulk sensitivity, shown below, largely confirmed this hypothesis.

A periodic array can act as a grating and provide wave vector components along the *x*- and *y*-axes; these components are able to excite the SPP-BWs and Wood's anomalies (WAs).[11,15] For a triangular lattice, the free space resonant wavelengths of the SPPs can be described by the plasmonic dispersion equation:

$$\lambda_r = \alpha\sqrt{\frac{3\varepsilon_d(\omega)\varepsilon_m(\omega)}{4[(\varepsilon_d(\omega)+\varepsilon_m(\omega))+(i^2+j^2+ij)]}} \quad (1)$$

where $\varepsilon_d(\omega)$ and $\varepsilon_m(\omega)$ are the frequency-dependent permittivities of the dielectric and the metal, respectively; α is the lattice constant; and i and j are integers for the corresponding reciprocal vector. The SPP waves that propagate at the interface between the dielectric and the metal are called SPP-BWs. The SPP-BWs are originally associated with the light transmission maxima where the well-known phenomenon of extraordinary optical transmission occurs.

As mentioned above, in addition to SPP-BWs, WAs can also occur in the transmission that is given by:

$$\lambda_{WA} = \alpha\sqrt{\frac{3\varepsilon_d(\omega)}{4(i^2+j^2+ij)}} \quad (2)$$

where m and n are the integers for the corresponding reciprocal vector, respectively. WAs can be described as diffractive and nonplasmonic features that propagate parallel to the surface. While SPP-BWs are originally associated with light transmission maxima, the wavelengths corresponding to the WA excitations are often the dips adjacent to those of the SPP-BWs, as can be seen from Fig. 3, which shows a Fano-like resonance profile consisting of dips close to the transmission peaks predicted by eqn (1).

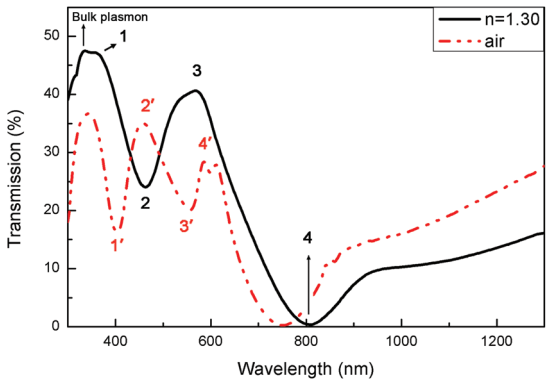

Fig. 3 Transmissions of a nanopillar array in a liquid (1.3 RIU, black) and in air (red) using back incident light.

Optical measurement

Fig. 3 shows the transmission spectra of a PNPA when surrounded by air and in a liquid (1.3 RIU) from the glass side. We refer to the propagation modes at the air–metal, substrate–metal, and refractive index liquid–metal interfaces as $(ij)_{air}$, $(ij)_{sub}$, and $(ij)_n$, respectively. The resonant wavelengths of the SPP-BWs were estimated using eqn (1) and using the dielectric function of Ag from a data book.[32] The locations of the WA modes were estimated using eqn (2). It should be noted that, in Fig. 3, peak 2′ and peak 4′ originate from the substrate–metal interface and are for SPP-BW$(1.1)_{sub}$ and SPP-BW $(1.0)_{sub}$, respectively. The dips next to the SPP-BW peaks, namely, dip 1′ and dip 3′, can be attributed to WA$(1.0)_{air}$ and WA$(1.0)_{sub}$, respectively. These results are consistent with those of previous reports.[33] According to the equations above, at normal incidence in a medium with a refractive index of 1.3 RIU, the wavelengths of SPP-BW$(1.1)_{1.3}$, SPP-BW$(1.0)_{1.3}$ and WA $(1.0)_{1.3}$ are 387 (peak 1), 549 (peak 3), and 506 (dip 2) nm, respectively. These calculated wavelengths are in good agreement with the experimental ones, confirming that the peaks originate from the SPP-BWs at the liquid–metal interface and that dip 2 originates from WA(1.0) at the liquid–metal interface.

By the comparing the simulation and experimental results, one can infer that, in the case of back incident lighting, the metal nanohole array exhibits better optical properties; however, there are still interactions between the metal nanohole array and the upper metal nanodisk array. Even though the PNPA structure differs from a normal metal nanohole array with an additional metal nanodisk array, its optical response is quite similar to that of a nanohole array. This is why a description in terms of a perfect metal nanohole array is sufficient in this case. The transmission symmetry was also studied by reversing the direction of light propagation. In both cases, that is, irrespective of whether the light was irradiated from the glass side or the front side, we did not observe any noticeable differences in the transmissions. This result is consistent with the reciprocating property of the PNPA structure (see ESI, Fig. S4†).[34]

Bulk sensitivity test

To examine the bulk sensitivity of the PNPA device as a refractive index sensor, we performed transmittance measurements at normal incidence from the backside. The bulk sensitivity was measured using Cargille index fluids. The standard liquids, which had refractive indices of 1.30–1.39 in steps of 0.01, were introduced within the PNPA (see ESI, Fig. S5†).

As mentioned above, we expected that the coupling effect of SRSPP and LSPR would offer better sensitivity than $WA(1.0)_n$. Thus, we examined the resonance shifts of both further. To be able to see clearly the shift in the spectra of D2 and D4 in Fig. 3, we plotted their normalized transmission spectra (Fig. 4a). An increase in the refractive index of the surrounding medium increased the resonant wavelength. The shifts in the spectral positions of D2 and D4 *versus* the refractive index are plotted in Fig. 4b using linear fitting. As expected, a higher refractive index sensitivity, of 375 nm RIU^{-1}, was obtained from D4, because of the coupling between the LSPR of the metal nanodisks and the SRSPPs of the metal nanohole array. This value was much higher than that of the SRSPPs that did not exhibit coupling with metal nanodisks (225 nm RIU^{-1}, see ESI, Fig. S6†). Thus, for the purposes of refractive index sensing, the PNPA exhibited better sensitivity than that of conventional SWHA-based sensors.[28]

The sensitivity of D2 was 155.6 nm RIU^{-1} only. Thus, on the basis of the bulk sensitivity measurements, it could be concluded that D4 exhibited better performance than did D2. This improvement in performance is most likely owing to a combination of factors. The first is surface plasmon matching: the nanodisk and nanohole arrays both have plasmon resonant modes, namely, the LSPR and the SRSPPs, respectively, at D4; these couple to each other, as can be confirmed from the broader line width of D4 in Fig. 3. Next, the electrical field distribution of D4 has a larger accessible hotspot region (Fig. 2f), resulting in a higher sensitivity. In the case of D2, because the electrical field distribution is concentrated mainly within the resist pillar (Fig. 2d), the sensitivity is lower. The figure of merit (FOM) was calculated as the sensitivity divided by the full width half maximum of the dip; its values were 3.13 and 1.66 for D4 and D2, respectively. Thus, we can conclude that a combination of effects attributable to the LSPR and the SRSPPs result in better refractive index sensitivity but a low FOM, since the line width is greater.

In order to realize a simple and low-cost sensor to determine the refractive indices of the surrounding media, we obtained the bright-field optical images of the PNPAs using a commercial microscopy system equipped with a CCD camera. Fig. 5a shows the bright-field microscopy images of the PNPAs as the refractive index of the surrounding medium was changed. The corresponding variation in the color of the reflected images can be seen clearly, as the reflective spectrum

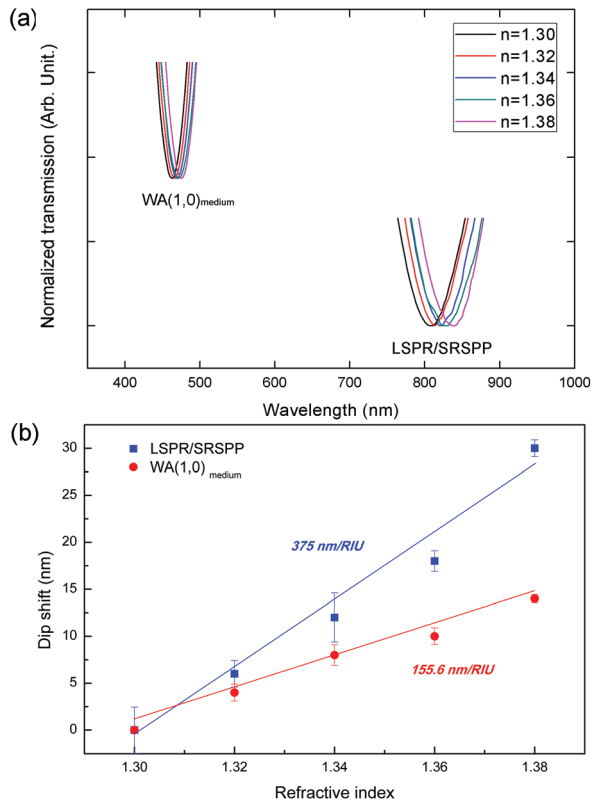

Fig. 4 (a) Normalized WA(1.0)medium and LSPR/SRSPP transmissions of a nanopillar array when surrounded by media with different refractive indices. (b) The dip shifts corresponding to the different refractive indices. The lines were linear fitted to WA(1.0)medium and LSPR/SRSPP, with the sensitivities being 155.6 nm RIU^{-1} and 375 nm RIU^{-1}, respectively.

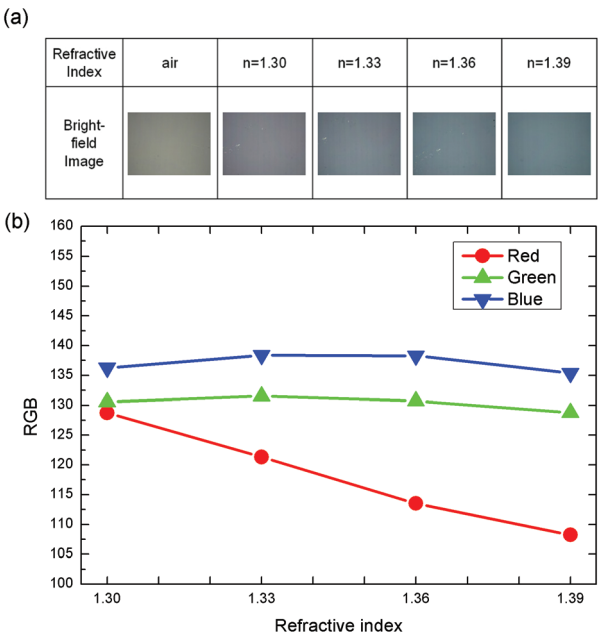

Fig. 5 (a) Bright-field optical microscopy images of PNPAs. The PNPAs with different media appear in different colors. (b) RGB values of the color components of the different surrounding media, as determined from the reflected colors.

was designed to fit within the visible region by choosing the appropriate thickness and type of the surface-plasmon active metal layer. Thus, a simple refractive index sensor could be realized by obtaining images using a camera and by subsequently analyzing the reflected colors. In order to quantify the sensitivity of the change in the color with the refractive index of the surrounding liquid, the images were decomposed into their additive RGB components. We found that the *R*-value decreased linearly with an increase in the refractive index, while the *G*- and *B*-values did not change appreciably, as shown in Fig. 5b. The sensitivity is calculated as the average change of $(\Delta R)^2 + (\Delta G)^2 + (\Delta B)^2$ *versus* the change of the refractive index of the surrounding media.[35] A sensitivity of 4700 was achieved. During the measurements, we cleaned the sample with deionized water to prevent damage to the PMMA structure, and subsequently blow-dried it before introducing the next refractive liquid. The experiments exhibited a high degree of repeatability.

We would like to mention that other similar plasmonic nanostructure sensors have been reported recently; these sensors exhibited a sensitivity as high as 900–1000 nm RIU^{-1} owing to interference between LSPRs and WA,[36] and plasmonic out-of-plane resonance.[37] Further, these plasmonic structures could be fabricated easily. In the case of these sensors, the most sensitive sensing spectral region was 1200–1400 nm for refractive indices of 1.3–1.4; in contrast, for the PNPA sensor synthesized in the present study, the most sensitive sensing spectral region was 800–850 nm. This allows for a lowering of the cost of the experimental setup, as the cost of a spectrometer that can be used for wavelengths of 800–850 nm is much lower than that of one that can be used for wavelengths of 1200–1400 nm.

Conclusions

In summary, a 3D nanostructure consisting of a metal nanodisk array supported on resist nanopillars with a perforated metal layer underneath was fabricated by thermal NIL for refractive index sensing. The fabricated device was tested through experiments and simulations. The lifted metal nanodisks supported by the nanopillars provided a larger accessible hotspot region for the surrounding environment, resulting in improved sensing capability. The sensing mechanism of this device is based on WAs and the coupling effect between the LSPR of the nanodisks and the SRSPPs of the nanoholes. Because of this coupling effect, the device had a larger accessible hotspot region compared to that of a WA(1.0)*n*-based device, in which the hotspot region was concentrated within the PMMA pillars. This was confirmed through numerical simulations. Furthermore, the fabricated device exhibited a better sensitivity (375 nm RIU^{-1}) than did the WA(1.0)*n*-based on (155.6 nm RIU^{-1}) and the noncoupling SRSPPs (225 nm RIU^{-1}). Finally, we demonstrated a simple sensing platform by analyzing the perceptible change in the color of the sensor for liquids with different refractive indices using optical microscopy; a sensitivity of 4700 was achieved. This device can be fabricated cost effectively and provides a new platform for label-free chemical and biomedical quantitative sensing with high sensitivity.

Acknowledgements

This work was funded by the German Research Foundation as Research Training Group "Nano- and Biotechnologies for Packaging of Electronic System" (DFG 1401/1-2). The authors thank Mr Ulrich Merkel and IHM TUD for equipment support.

Notes and references

1 J. Homola, S. S. Yee and G. Gauglitz, *Sens. Actuators, B*, 1999, **54**, 3–15.
2 S. Lal, S. Link and N. J. Halas, *Nat. Photonics*, 2007, **1**, 641–648.
3 G. G. Nenninger, P. Tobiska, J. Homola and S. S. Yee, *Sens. Actuators, B*, 2001, **74**, 145–151.
4 C. L. Baird and D. G. Myszka, *J. Mol. Recognit.*, 2011, **14**(5), 261–268.
5 E. Kretschm and H. Raether, *Z. Naturforsch., A: Astrophys. Phys. Phys. Chem.*, 1968, **A23**(12), 2135.
6 C. Ropers, C. C. Neacsu, T. Elsaesser, M. Albrecht, M. B. Raschke and C. Lienau, *Nano Lett.*, 2007, **7**(9), 2784–2788.
7 M. Stewart, C. Anderton, L. Thompson, J. Maria, S. Gray, J. Rogers and R. Nuzzo, *Chem. Rev.*, 2008, **108**(2), 494–521.
8 A. J. Haes and R. P. Van Duyne, *Expert Rev. Mol. Diagn.*, 2004, **4**(4), 527–537.
9 A. Gomez-Hens, J. Fernandez-Romero and M. P. Aguilar-Caballos, *Trends Anal. Chem.*, 2008, **27**(5), 394–406.
10 S. W. Lee, K. S. Lee, J. Ahn, J. J. Lee, M. G. Kim and Y. B. Shin, *ACS Nano*, 2011, **5**(2), 897–904.
11 T. W. Ebbesen, H. J. Lezec, H. F. Ghaemi, T. Thio and P. A. Wolff, *Nature*, 1998, **391**, 667–669.
12 W. L. Barnes, W. A. Murray, J. Dintinger, E. Devaux and T. W. Ebbesen, *Phys. Rev. Lett.*, 2004, **92**, 107401.
13 I. J. H. McCrindle, J. Grant, T. D. Drysdale and D. R. S. Cumming, *Adv. Opt. Mater.*, 2014, **2**(2), 149–153.
14 J. C. Sharpe, J. S. Mitchell, L. Lin, N. Sedoglavich and R. J. Blaikie, *Anal. Chem.*, 2008, **80**(6), 2244–2249.
15 M. E. Stewart, N. H. Mack, V. Malyarchuk, J. A. N. T. Soares, T. W. Lee, S. K. Gray, R. G. Nuzzo and J. A. Rogers, *Proc. Natl. Acad. Sci. U. S. A.*, 2006, **103**(46), 17143–17148.
16 A. Degiron, H. J. Lezec, W. L. Barnes and T. W. Ebbesen, *Appl. Phys. Lett.*, 2002, **81**, 4327.
17 J. Braun, B. Gompf, G. Kobiela and M. Dressel, *Phys. Rev. Lett.*, 2009, **103**, 203901.
18 J. W. Menezes, J. Ferreira, M. J. L. Santos, L. Cescato and A. G. Brolo, *Adv. Funct. Mater.*, 2010, **20**(22), 3918–3924.

19 T. R. Jensen, M. D. Malinsky, C. L. Haynes and R. P. Van Duyne, *J. Phys. Chem. B*, 2000, **104**(45), 10549–10556.
20 K. L. Lee, P. W. Chen, S. H. Wu, J. B. Huang, S. Y. Yang and P. K. Wei, *ACS Nano*, 2012, **6**(4), 2931–2939.
21 V. Malyarchuk, F. Hua, N. H. Mack, V. T. Velasquez, J. O. White, R. G. Nuzzo and J. A. Rogers, *Opt. Express*, 2005, **13**, 5669–5675.
22 W. Wu, W. M. Tong, J. Bartman, Y. F. Chen, R. Walmsley, Z. N. Yu, Q. F. Xia, I. Park, C. Picciotto, J. Gao, S. Y. Wang, D. Morecroft, J. Yang, K. K. Berggren and R. S. Williams, *Nano Lett.*, 2008, **8**(11), 3865–3869.
23 H. K. Cho, J. Jang, J. H. Choi, J. Choi, J. Kim, J. S. Lee, B. Lee, Y. H. Choe, K. D. Lee, S. H. Kim, K. Lee, S. K. Kim and Y. H. Lee, *Opt. Express*, 2006, **14**(19), 8654–8660.
24 L. Teng, A. Finn, M. Plötnera, H. Shia and W. Fischer, *Microelectron. Eng.*, 2014, **121**, 27–32.
25 X. G. Liang, K. J. Morton, R. H. Austin and S. Y. Chou, *Nano Lett.*, 2007, **7**(12), 3774–3780.
26 J. J. Mock, D. R. Smith and S. Schultz, *Nano Lett.*, 2003, **3** (4), 485–491.
27 M. M. Miller and A. A. Lazarides, *J. Opt. A: Pure Appl. Opt.*, 2006, **8**, 239.
28 J. Henzie, M. H. Lee and T. W. Odom, *Nat. Nanotechnol.*, 2007, **2**, 549–554.
29 M. Khorasaninejad, S. M. Raeis-Zadeh, H. Amarloo, N. Abedzadeh, S. Safavi-Naeini and S. S. Saini, *Nanotechnology*, 2013, **24**(35), 355501.
30 A. Dmitriev, C. Hagglund, S. Chen, H. Fredriksson, T. Pakizeh, M. Kall and D. S. Sutherland, *Nano Lett.*, 2008, **8**, 3893–3898.
31 N. Large, J. Aizpurua, V. K. Lin, S. L. Teo, R. Marty, S. Tripathy and A. Mlayah, *Opt. Express*, 2011, **19**, 5587–5595.
32 E. D. Palik, *Handbook of Optical Constants of Solids*, Academic Press, New York, 1985.
33 H. E. Arabi, M. Park, M. Pournoury and K. Oh, *Opt. Express*, 2011, **19**(9), 8514–8525.
34 W. D. Li, J. Hu and S. Y. Chou, *Opt. Express*, 2011, **19**(21), 21098–21108.
35 M. Khorasaninejad, N. Abedzadeh, J. Walia, S. Patchett and S. S. Saini, *Nano Lett.*, 2012, **12**(8), 4228–4234.
36 Y. Shen, J. Zhou, T. Liu, Y. Tao, R. Jiang, M. Liu, G. Xiao, J. Zhu, Z.-K. Zhou, X. Wang, C. Jin and J. Wang, *Nat. Commun.*, 2013, **4**, 2381.
37 F. Zhao, J. Zeng, M. M. P. Arnob, P. Sun, J. Qi, J. C. Wolfe, P. Motwani, M. Gheewala, T. R. Lee, C.-H. Li, R. Willson, U. Strych, A. Paterson, B. Raja and W.-C. Shih, *Nanoscale*, 2014, **6**, 8199–8207.